nature astronomy

Article

https://doi.org/10.1038/s41550-023-02120-8

An aspherical distribution for the explosive burning ash of core-collapse supernovae

Received: 23 February 2023

Accepted: 2 October 2023

Published online: 26 October 2023

Check for updates

Qiliang Fang[1] ✉, Keiichi Maeda[1] ✉, Hanindyo Kuncarayakti[2,3] & Takashi Nagao[2,4,5]

It is widely believed that asphericity in the explosion is the crucial ingredient leading to successful core-collapse (CC) supernovae. However, direct observational evidence for the explosion geometry and for the connection with the progenitor properties are still missing. Based on the thus-far largest late-phase spectroscopic sample of stripped-envelope CC supernovae, we demonstrate that about half of the explosions exhibit a substantial deviation from sphericity. For these aspherical CC supernovae, the spatial distributions of the oxygen-burning ash and the unburnt oxygen, as traced by the profiles of [Ca II] λλ7291,7323 and [O I] λλ6300,6363 emissions, respectively, appear to be anticorrelated, which can be explained if the explosion is bipolar and the oxygen-rich material burnt into two detached iron-rich bubbles. Our combined analysis of the explosion geometry and the progenitor mass further suggests that the degree of asphericity grows with the mass of the carbon–oxygen core, which may be used to guide state-of-the-art simulations of CC supernova explosions.

When the nuclear fuel deep inside a massive star (with a zero-age main-sequence mass $>8\,M_{\odot}$) is exhausted, the core collapses to form a neutron star or a black hole. A large amount of gravitational energy is released, part of which is transformed into the kinetic energy that drives the expulsion of the rest of the star, leading to a core-collapse (CC) supernova.

The mechanism behind a CC supernova is one of the main long-standing challenges in astrophysics. Studying the geometry of the explosion and the relation with the mass of the progenitor may shed light on this unresolved issue. If the released energy is concentrated in a specific direction, the explosion has a bipolar configuration[1,2]. During this process, the oxygen-rich materials are compressed to the equatorial plane, whereas the explosive burning takes place along the axis perpendicular to the oxygen-rich plane[3,4]. Bipolar explosions are of particular interest due to their potential connection with gamma-ray bursts (GRBs). The latter produce a collimated relativistic beam and can be observed only when viewed on-axis[5].

The late-phase (nebular) spectroscopy of stripped-envelope (SE) supernovae (a subtype of CC supernovae) is a unique tool for studying the geometry of the innermost ejecta. An SE supernova is produced by a massive star that lost most of its hydrogen envelope before the explosion[6]. Several months after the explosion, the ejecta of an SE supernova becomes optically thin due to its expansion. As it no longer hidden by the massive envelope, the central region is exposed. During this phase, the spectrum of an SE supernova is dominated by forbidden lines, in particular [O I] λλ6300,6363 and [Ca II] λλ7291,7323 (Fig. 1). Research works in the past focused on [O I] emitted from the unburnt oxygen-rich stellar material, the profile of which strongly depends on the viewing angle if the explosion is aspherical[7,8]. The double-peaked [O I], a distinct feature of a bipolar explosion, has been found to be common for SE supernovae[9]. This result has been verified with larger samples[10–13]. However, there is a dilemma when inferring the geometry of the explosion using only [O I]: (1) When viewed from the on-axis direction, [O I] will appear to be sharp and single-peaked, making it indistinguishable from a spherical explosion. (2) Observing the double-peaked [O I], which is the smoking gun of a bipolar explosion, suggests the explosion has been viewed on-edge, hiding its possible connection with a GRB[7].

---

[1]Department of Astronomy, Kyoto University, Kyoto, Japan. [2]Tuorla Observatory, Department of Physics and Astronomy, University of Turku, Turku, Finland. [3]Finnish Centre for Astronomy with ESO (FINCA), University of Turku, Turku, Finland. [4]Aalto University Metsähovi Radio Observatory, Kylmälä, Finland. [5]Aalto University Department of Electronics and Nanoengineering, AALTO, Espoo, Finland. ✉e-mail: fangql@kusastro.kyoto-u.ac.jp; keiichi.maeda@kusastro.kyoto-u.ac.jp

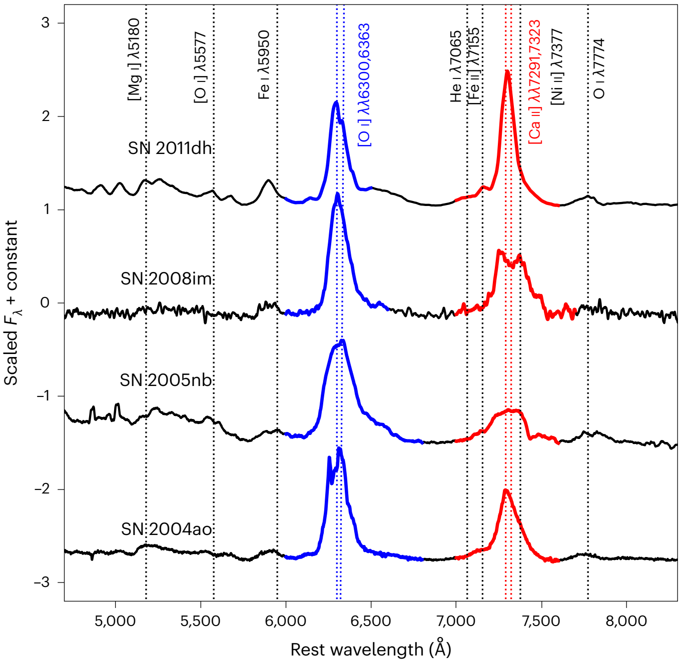

Fig. 1 | Nebular spectroscopy of SE supernovae. The ranges of [O I] (blue) and [Ca II] (red) are highlighted. From top to bottom: SN 2011dh (SP [O I] and [Ca II]), SN 2008im (SP [O I] and horn-like [Ca II]), SN 2005nb (SP [O I] and flat-topped [Ca II]) and SN 2004ao (horn-like [O I] and SP [Ca II]). The central wavelengths of the typical nebular emissions are labelled by the vertical lines.

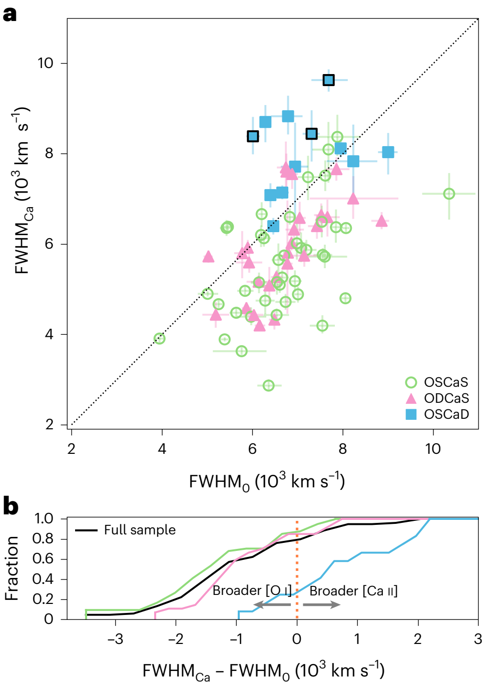

Fig. 2 | Analysis of the linewidths. a, Relation between the FWHMs of [O I] and [Ca II]. Objects in the different line profile categories (classified by the profiles of [O I] and [Ca II]) are labelled by different colours and markers (OSCaS: both [O I] and [Ca II] are single-peaked; ODCaS: [O I] is double-peaked and [Ca II] is single-peaked; OSCaD: [O I] is single-peaked and [Ca II] is double-peaked). Objects with the horn-like [Ca II] profiles are highlighted by the thick edges. Data are presented as mean value with error bars indicating the 16th and 84th percentiles. **b**, Statistics of the difference in linewidths. The cumulative distributions of the difference in [Ca II] and [O I] widths for objects in different line profile categories are compared.

(3) Further, an interpretation of a two-dimensional configuration based on a one-dimensional line profile is degenerate[11–13]. We, therefore, need an improved method to infer the explosion geometry, especially the characteristic features when a bipolar explosion is viewed on-axis.

When a CC supernova explosion occurs, oxygen is burnt into iron-peak elements in the direction in which a large amount of the energy is released. Outside this region, the material is still oxygen-rich and the fractions of the heavy elements are negligible. The explosive burning ash and the unburnt material are, therefore, decoupled geometrically. The relation of the profiles of the emission lines originating in these two regions is, thus, a good probe of the explosion geometry. [O I] has been frequently employed to infer the geometry of the unburnt oxygen-rich material, whereas [Ca II], which is strong in most SE supernovae, is the main coolant of the oxygen-burning ash, making it an ideal tool for tracing the configuration of the explosion-made region[14–18].

In this work, we propose combining the analyses of the [O I] and [Ca II] profiles to infer the geometry of the explosion. Horn-like and flat-topped profiles in either of the two lines are considered to be signatures of an aspherical explosion. Hereafter, these are collectively referred to as double-peaked (DP) profiles to distinguish them from single-peaked (SP) profiles. We study the nebular spectra of 80 SE supernovae. Among these objects, 41 are single-peaked [O I] and single-peaked [Ca II] (OSCaS). For objects considered to have experienced a bipolar explosion (that is, with either double-peaked [O I] or double-peaked [Ca II]), the [O I] and [Ca II] profiles appear to be anticorrelated. Thus, 27 objects have double-peaked [O I] and single-peaked [Ca II] (ODCaS) whereas 12 objects have single-peaked [O I] and double-peaked [Ca II] (OSCaD). Some examples of supernovae in different line profile categories are shown in Fig. 1. The anticorrelation of the [O I] and [Ca II] profiles can be understood as similar explosion configurations being viewed from different angles. These bipolar explosions are characterized by burning ash distributed along a specific axis and are surrounded by an oxygen-rich torus. When viewed on-axis, the Doppler shifts of the bipolar calcium elements give rise to the horn-like profile of [Ca II], whereas most of the oxygen elements on the torus are moving perpendicularly to the line of sight (LOS), producing single-peaked [O I]. On the other hand, when viewed from a direction perpendicular to the axis, [O I] appears to be horn-like and [Ca II] is single-peaked for a similar reason. This simple picture is supported further by the data: (1) the line profiles are largely either single-peaked or double-peaked and (2) there is no object showing both horn-like [O I] and horn-like [Ca II].

Evidence of asphericity can also be inferred from the widths of [O I] and [Ca II]. Since the velocity of the material is proportional to the radial coordinate under the assumption of homologous expansion, the width of a line reflects the spatial extension of the emitting elements along the LOS[11,13,14,16,18]. The full-widths at half-maximum (FWHMs) of [O I] and [Ca II] are compared in Fig. 2a. For the OSCaS and ODCaS objects, [O I] is broader than [Ca II] in more than 80% of cases. In contrast, for OSCaD objects, [Ca II] is broader than [O I] in most cases. The difference between the [Ca II] and [O I] widths is shown in Fig. 2b. The OSCaD objects have distinct population from the other two types, with $P < 0.001$ from the Anderson–Darling test. The large FWHMs of [Ca II] are not consistent with a spherical explosion in which heavier elements are explosively synthesized in inner regions and expelled at lower velocities. However, these data can be naturally explained by a bipolar explosion in which heavy elements are synthesized along a specific axis and ejected at high velocities. If viewed closely from the axis, the average LOS velocity of the iron-rich ash may be faster than that of the oxygen-rich material, resulting in broader [Ca II][4].

The peculiar double-peaked profile of the [Ca II], along with its broadness, strongly suggests a bipolar distribution in the emitting

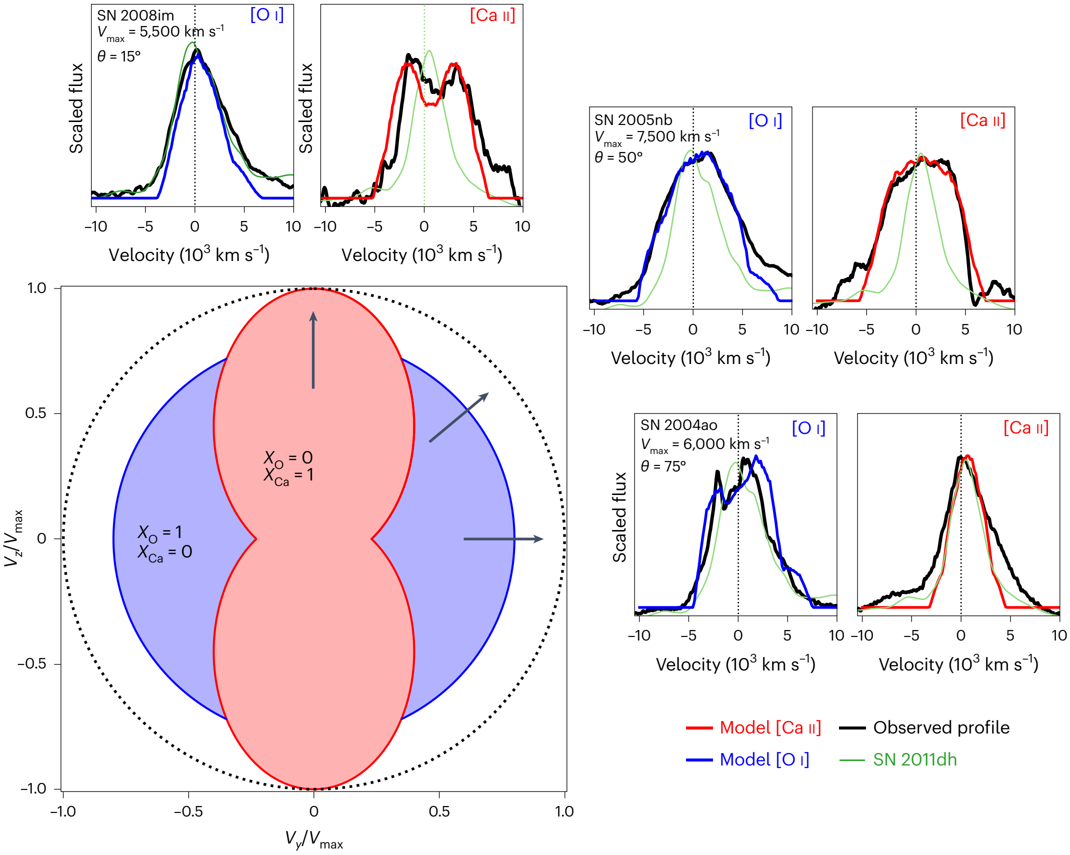

Fig. 3 | Configuration of the idealized axisymmetric model. The O-rich region (labelled by blue) and the iron/calcium-rich ash (labelled by red) are complementary in their distributions. The profiles given by the model for [O I] (blue) and [Ca II] (red) strongly depend on the viewing angle, which are compared with the observed [O I] and [Ca II] profiles (black lines) of SN 2008im, SN 2005nb and SN 2004ao. In these panels, the [O I] and [Ca II] profiles of SN 2011dh, an OSCaS object, are plotted to illustrate the difference between the spherical and bipolar explosions.

region. We propose an idealized axisymmetric model to explain the profiles of the OSCaD and ODCaS objects (Fig. 3). The model is characterized by two separated zones: the calcium elements are distributed in a peanut-like region ($X_{\mathrm{O}} = 0$ and $X_{\mathrm{Ca}} = 1$, where X is the mass fraction), whereas outside this region, the material is oxygen-rich ($X_{\mathrm{O}} = 1$ and $X_{\mathrm{Ca}} = 0$). The physical properties (for example, mass fractions and γ-ray deposition rate) are assumed to be uniform in each zone for simplicity. No radiation transfer process is included. These simplifications allow us to focus on the geometric effect. When viewed from $\theta = 15°$, 50° or 75° from the axis, the model produces single-peaked [O I]/horn-like [Ca II], single-peaked [O I]/flat-topped [Ca II] and horn-like [O I]/single-peaked [Ca II], respectively, in good agreement with the observed profiles of SN 2008im, SN 2005nb and SN 2004ao, which are shown in Fig. 3 as examples. It is surprising that such a simple model involving only two parameters (the maximum velocity V_{max} and the viewing angle θ) can explain the wide range of both the [O I] and [Ca II] profiles simultaneously, as well as their anticorrelation. This result suggests that the geometric effect is responsible for the diversity seen in the line profiles. Including other ingredients (for example, the density distribution and radiation transfer) may improve the agreement with the observations, although their roles are probably secondary.

Statistics is useful for constraining the explosion geometry. The occurrence rate of bipolar explosions ($N_{\mathrm{Bipolar}} = N_{\mathrm{DP\,[Ca\,II]}} + N_{\mathrm{DP\,[O\,I]}}$) is 0.49 (= 39/80), implying that about half of SE supernovae explode with a non-negligible departure from a spherical configuration. Here $N_{\mathrm{DP\,[O\,I]}}$ and $N_{\mathrm{DP\,[Ca\,II]}}$ are the numbers of objects showing double-peaked [O I] and double-peaked [Ca II], respectively. Within this bipolar explosion category, the occurrence rate of double-peaked [Ca II] is 0.31 (= 12/39), which is consistent with the axisymmetric model: at $\theta \simeq 45°$, the [Ca II] profile transforms from double-peaked to single-peaked. If there is no bias in the orientation, the expected occurrence rate of double-peaked [Ca II] in this model is 0.29 ± 0.06 for this sample size, assuming that the solid angle is uniformly distributed.

The dependency of the explosion geometry on the progenitor mass is crucial for revealing the explosion mechanism of CC supernovae. However, observational hints are still missing. In this work, we employ the intensity ratio of [O I] to [Ca II] (hereafter denoted as [O I]/[Ca II]) as a proxy for the CO core mass under the assumption that the amount of burning ash is not sensitively dependent on the CO core mass. This relation has been routinely adopted in previous theoretical and observational works, with a larger [O I]/[Ca II] implying a more massive CO core[13–15,19–23]. To investigate the relation between [O I]/[Ca II] and the asphericity of the explosion, the sample was binned into ten groups according to the [O I]/[Ca II] sequence. The range of [O I]/[Ca II] for the bins is −0.3 to 0.6 in a logarithmic scale, which roughly corresponds to a CO core mass of 2.05 to 7.84 $M_{\odot}$ or a zero-age main-sequence mass of 12 to 30 $M_{\odot}$, based on the scaling relations between these quantities[20,24]. The relation between [O I]/[Ca II] and the bipolar rate ($N_{\mathrm{DP\,[Ca\,II]}} + N_{\mathrm{DP\,[O\,I]}}$ divided by the total number of the objects) in each group was investigated, and no correlation was discerned (Spearman correlation coefficient $\rho = 0.03$), as shown in Fig. 4a.

The lack of correlation between the bipolar rate and [O I]/[Ca II] possibly suggests that whether a CC supernovae explodes in a spherical or bipolar configuration is not determined by its CO core mass. However, the association of [O I]/[Ca II] to the CO core mass requires further quantification; for example, if the explosion energy tends to be

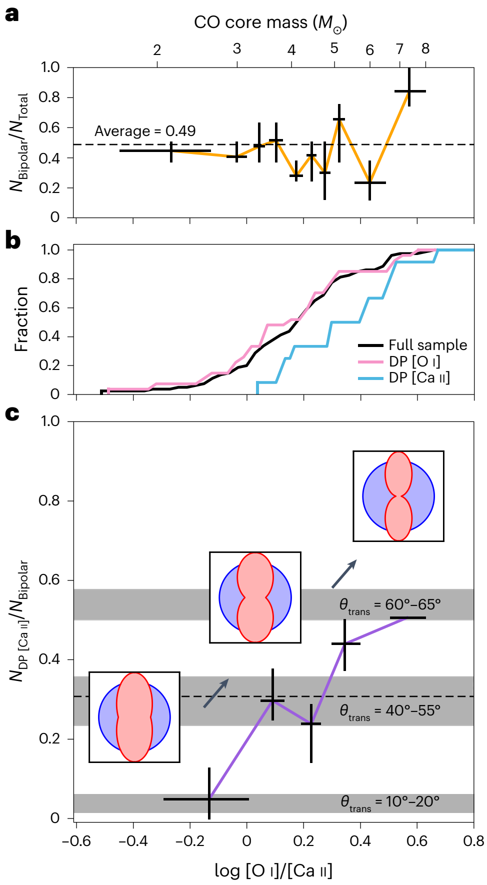

Fig. 4 | The relation between the explosion geometry and the CO core mass of the progenitor. **a**, Occurrence rate of bipolar supernovae as a function of [O I]/[Ca II]. The bipolar rate of the full sample (0.49) is indicated by the dashed line. **b**, Cumulative distribution of [O I]/[Ca II] for different line profile categories. The ratio of the full sample (black), double-peaked [O I] (pink) and double-peaked [Ca II] (light blue) are compared. **c**, Occurrence rate of double-peaked [Ca II] as a function of [O I]/[Ca II]. The insets schematically illustrate a sequence for the explosion geometry as a function of the CO core mass, which explains the observed relation. The three models have different transition angels $\theta_{\rm trans}$. When viewed above this angle, the [Ca II] profile transforms from double-peaked to single-peaked. The shaded regions mark the expected double-peaked [Ca II] rates of these models assuming a uniform distribution of the solid angle. In **a** and **c**, data are presented as mean value with error bars indicating the 16th and 84th percentiles.

larger for a more massive CO core[3,13,24,25], thus creating a larger amount of Ca (ref. 26,27), this relation may be diluted. In any case, the statistical investigation presented here indicates that a common explosion mechanism is behind CC supernovae across a range of CO core masses, at least for the sample of canonical SE supernovae studied in the current work. The asphericity of the energy release must be key to producing CC supernovae, with about half of the sample having a detectable bipolar distribution, as seen for either [O I] or [Ca II].

A similar analysis was applied separately to the bipolar sample. The cumulative distributions of [O I]/[Ca II] of the OSCaD and ODCaS objects are compared with the full sample in Fig. 4b. Surprisingly, the objects with double-peaked [Ca II] have a larger [O I]/[Ca II] ratio than those with double-peaked [O I] ($P < 0.05$ from the Anderson–Darling test). In the low [O I]/[Ca II] range, the presence of double-peaked [O I] suggests that the explosion is bipolar. The iron-rich bubbles that characterize the geometry of the burning ash are not distinctly separated into two hemispheres, as inferred from the absence of double-peaked [Ca II]. By binning the bipolar supernovae into five groups according to the [O I]/[Ca II] sequence, we find a trend in which the occurrence rate of the double-peaked [Ca II] in each group increases with the average [O I]/[Ca II] ($\rho = 0.87$ and $P = 0.053$; Fig. 4c), although the statistics is limited by the relatively small number in each bin ($n \approx 8$) and should be considered as suggestive[28]. This tendency can be explained if the transition angle $\theta_{\rm trans}$ increases with [O I]/[Ca II]. Above this angle, the [Ca II] profile transforms from double-peaked to single-peaked. This is consistent with a scenario in which the explosion becomes more aspherical and the burning ash becomes more detached and more collimated as the CO core grows, which is schematically demonstrated in Fig. 4c.

The correlation of the occurrence rate of double-peaked [Ca II] (Fig. 4c) and the probable non-correlation of the occurrence rate of the aspherical explosions (Fig. 4a) to the CO core mass (or the explosion energy, due to its correlation with the kinetic energy $E_{\rm K}$ of the ejecta[13,24]) must be satisfied in the explosion mechanism(s). The standard delayed-neutrino explosion mechanism involves various instabilities[29], some of which may introduce a bipolar configuration (for example, standing accretion shock instabilities[30,31]). Recent simulations further show that either rotation or a magnetic field, or both, may have an important role in assisting a neutrino-driven explosion[32,33]. These effects may naturally introduce a specific direction in the explosion dynamics. In a massive core, the neutrino-driven mechanism alone would be insufficient to overcome the binding energy[29], and then the rotation and magnetic field may become important even energetically, so that there is a magneto-rotational explosion[34].

Methods

Sample description

The SE supernova sample in this work is the same as that used in ref. 13, which was mainly compiled from the literature[35,36]. The analysis was restricted to nebular spectra acquired not less than 100 days after the discovery of the supernova. In this sample, 80 objects have spectra with a high enough signal-to-noise ratio to allow an investigation of both the [O I] $\lambda\lambda$6300,6363 and [Ca II] $\lambda\lambda$7291,7323 profiles. These were selected for further analysis. Supernovae associated with a GRB or X-ray flash (XRF, a low-energy analogue of a GRB), namely SN 1998bw/GRB 980425 and SN 2006aj/XRF 060218, were excluded from the analysis to avoid introducing any bias in the orientation[37–40]. SN 2012ap, which is suggested to be a GRB-associated supernova but viewed off-axis, was also excluded[41,42]. The peculiar SN 2005bf, whose explosion mechanism is probably different from that of a normal SE supernovae, was not included either[9,43]. The SE supernovae studied in this work are listed in Supplementary Table 1.

Linewidth measurement and error estimation

Before measuring the linewidths of [O I] and [Ca II], the nebular spectrum was first corrected for the redshift, which was derived from the central wavelengths of the narrow emission lines from the explosion site or the redshift of the host galaxy[44]. The next step was to remove the underlying continuum following the same method as used in previous works[13,22,45]. The line connecting the minima at both sides of the emission was defined to be the local continuum and then excised, as illustrated in Supplementary Fig. 1.

To derive the isolated [O I], we needed to subtract the broad Hα-like structure at the red wing of [O I]. This emission was assumed to be symmetric with respect to 6,563 Å and was constructed by reflecting the red side to the blue side. A similar procedure was applied to derive the [Ca II] profiles, which were complicated by the many emissions at similar wavelength ranges emitted by the iron-peak elements. However, most of these lines were usually very weak compared with [Ca II] and were not taken into consideration to avoid complications. We first subtracted the He I λ7065 line by assuming that it was symmetric with respect to the central wavelength. The profile was constructed by reflecting the blue side to the red side. After He I was subtracted, the profile of [Fe I] λ7155 was constructed with the same method.

The separation of the central wavelengths of [Fe I] and [Ca II] was ~5,700 km s^{-1}, whereas the half-width at half-maximum of [Ca II] was always smaller than ~5,000 km s^{-1} (Fig. 2). The blue side of [Fe I] was, therefore, hardly contaminated by [Ca II]. It was difficult to remove [Ni II] λ7377 from the [Ca II] complex because its separation from the central wavelength of [Ca II] was small (~3,500 km s^{-1}). We assumed that [Ni II] and [Fe I] have the same profile and that the ratio of the intensities L_{7377}/L_{7155} was 0.6 (for the solar Ni/Fe ratio and temperature of the emission region, which was ~4,000 K, see refs. [46,47]). The profile for [Ca II] was derived by subtracting the He I, [Fe I] and [Ni II] profiles from the complex. Other contaminating lines were usually very weak compared with [Ca II], and they were not taken into consideration to avoid complications. The FWHM of the isolated [O I] and [Ca II] were then measured and corrected for instrumental broadening. Some examples of FWHM measurements are shown in Supplementary Fig. 1.

The uncertainty in the FWHM was estimated by employing a Monte Carlo method. An original spectrum was smoothed by convolving it with a boxcar filter. The smoothed spectrum was subtracted from the original one, then the standard deviation of the residual flux in the wavelength range 6,000 to 8,000 Å was estimated as the noise level of the spectrum. To generate a simulated spectrum, Gaussian noise was added to the spectrum using the estimated noise level. The end points of the local continuum, the central wavelengths of the Hα-like structure, He I, [Fe I] and [Ni II] were allowed to vary by ±600 km s^{-1} to account for the typical resolution of nebular spectroscopy, assuming flat distributions. The FWHM was then calculated following the method described above. This procedure was repeated 10^4 times, and the 16th and 84th percentiles of these measurements were estimated as the lower and upper limits of the FWHM.

Line morphology

The profiles of [O I] and [Ca II], being diverse in morphology, were employed to characterize the geometry of the emitting regions. Although the [O I] profile is typically categorized by multi-Gaussian fitting, this method has several limitations: (1) The results of the fitting can be degenerate, leading to an ambiguous interpretation of the profile. (2) The blending of emissions from iron-peak elements complicates the extension of this approach to [Ca II]. In this work, we employ the convolution method[48]. The line profiles of [O I] in SN 2008im and [Ca II] in SN 2011dh were employed as templates for single-peaked [O I] and [Ca II], respectively. These templates were convolved with Gaussian kernels by freely adjusting the centres and standard deviations until their widths matched those of the other objects to ensure proper comparison. Profiles that resembled the convolved template were classified as single-peaked. Alternatively, profiles that deviated from the convolved template but exhibited troughs at ~0 km s^{-1} and roughly symmetrical local peaks with respect to 0 km s^{-1} were categorized as horn-like. In the absence of these features, the profiles were classified as flat-topped. Note that flat-topped and horn-like profiles could not sometimes be unambiguously classified, especially when the troughs were shallow. However, the exact distinction between these two profiles was not essential to the analysis in this work. Therefore, the horn-like and flat-topped profiles were collectively referred to as double-peaked profiles. We neglected the substructures that occasionally emerge on the broad bases of the emissions and focused on the bulk properties. In practice, we found that this evaluation led to unambiguous classifications between single-peaked and double-peaked profiles. Several examples are given in Supplementary Fig. 2.

Axisymmetric model

Rather than working on multi-dimensional radiative transfer with a detailed treatment of the hydrodynamics and nucleosynthesis, we attempted to develop a simplified axisymmetric model that can reproduce the unique double-peaked profiles of [O I] and [Ca II] and their anticorrelation. The axisymmetric model is characterized by two separated zones: (1) The explosive burning ash is described by two symmetric (with respect to the plane perpendicular to the axis of symmetry), off-centre ellipsoids. The velocity of the edge of each ellipsoid is $V_{\max}$, the maximum velocity of the model. In this zone, the oxygen elements synthesized during stellar evolution are burnt into heavier elements, with $X_{\rm O} = 0$ and $X_{\rm Ca} = 1$ (as we are interested in only calcium, other iron-peak elements are not included). (2) The O-rich zone is enclosed in a sphere with radius $V_{\rm O} = 0.8V_{\max}$. We used $V_{\rm O} = 0.8V_{\max}$, as this value can well produce the widths of both [O I] and [Ca II] for most supernovae in the sample except for two objects, SN 2006T and SN 2012fh. The overlap of this sphere with the iron-rich ellipsoids was excised. This zone was filled with the unburnt material where the fractions of the iron-peak elements were negligible ($X_{\rm O} = 1$ and $X_{\rm Ca} = 0$). The mass fractions and the density were assumed to be homogeneous. Throughout the model construction, we used the velocity as a proxy of spatial coordinate. During the nebular phase, the ejecta dynamics is well characterized by homologous expansion, such that a grid point moves in the radial direction with a velocity proportional to its radial coordinate.

The above model was mapped onto a three-dimensional cube, which was divided into 500 × 500 × 500 cells using the Cartesian coordinates, with each side bounded by $-V_{\max}$ and $+V_{\max}$. No radiation transfer was introduced. The flux from each grid point was assumed to be proportional to its volume. Homologous expansion suggests that the infinitesimal volume dr^3 is proportional to its 'volume' dV^3 in velocity space. The specific flux of [O I] (or [Ca II]) $F_V dV$ at velocity V was calculated by summing dV^3 of the O-rich (or iron-rich) grid points with the LOS velocities within V to $V + dV$. [O I] is, by nature, a doublet, consisting of two transitions emitting at 6,300 and 6,363 Å, respectively. These two components, separated by ~3,000 km s^{-1}, have intensity ratio 3:1 in the optically thin limit. For the [Ca II] doublet, the two components, centred at 7,291 and 7,323 Å, are separated by ~1,300 km s^{-1}, and their intensity ratio was fixed to be 1:1 in the optically thin limit. The model [O I] and [Ca II] profiles, with $V_{\max} = 5{,}000$ km s^{-1} and viewing angle θ varying from 0° (on-axis) to 90° (on-edge), are shown in Supplementary Fig. 3.

The axisymmetric model predicts the unique features of both [O I] and [Ca II] profiles and their anticorrelation. The [O I] and [Ca II] profiles are determined by θ with the opposite tendency. When viewed from $\theta = 0°$ (on-axis), the model [Ca II] shows a horn-like profile and [O I] is single-peaked. When viewed from $\theta = 90°$ (on-edge), the [Ca II] profile becomes single-peaked and [O I] transforms to the horn-like profile.

Application of the model to the observations

In this section, the model profiles were applied to supernovae with either double-peaked [Ca II] or [O I] (except for SN 2015ah, which will be discussed later). We freely varied $V_{\max}$ and θ to find parameter values that corresponded to the observations. The procedure was as follows. For each object, we focused on the line that exhibited the double-peaked feature, that is, [O I] for the ODCaS category and [Ca II] for the OSCaD category. The viewing angle of the model was varied until the depth of the trough in the corresponding line matched the observation. Flat-topped profiles were an extreme case in which the trough depth was 0. After θ was fixed, we adjusted $V_{\max}$ until the widths of the observed double-peaked profile and the corresponding model profile matched. Any line that appeared to be single-peaked was not directly involved in this procedure but served to assess the alignment between the model and the observations. In two cases, SN 2006T and SN 2012ah, the third parameter, that is, the maximum velocity of the O-rich region $V_{\rm O}$, was required, although in most cases fixing $r_{\rm O}$ (= $V_{\rm O}/V_{\max}$) = 0.8 gave reasonable matches. The application of the model to the full sample of supernovae that are considered to be bipolar explosions is shown in Supplementary Fig. 4.

The [O I] and [Ca II] profiles from the simplified model indeed captured the main features of [O I] and [Ca II], although they failed to produce some substructures, which may require the introduction of clumpy structures (for example, a moving O-rich blob as exemplified by SN 1996aq; ref. 11) or a centrally concentrated density profile (SN 1990aj, SN 2002ap and SN 2006ck). For the horn-like [O I] profiles, the model predicts that the intensity of the peak at the redder wavelength is larger than the bluer one because of the contribution from the secondary component of the [O I] doublet centred at 6,363 Å (or 3,000 km s^{-1}). However, some objects had flat-topped profiles (for example, SN 1990U and SN 2005aj) or a stronger blue peak (SN 2000ew, SN 2004gt and SN iPTF13bvn). This could be explained by the effect of the residual opacity: a photon escaping from the far side of the ejecta experiences twice the scattering or absorption (see, for example, ref. 20), which will effectively reduce the fluxes at redder wavelengths. If the fluxes from the grid points with LOS velocity >0 were manually reduced by 10–40%, the model indeed produced [O I] with a flat-topped profile or a horn-like profile with a stronger blue peak.

In conclusion, the axisymmetric model can produce the [O I] and [Ca II] profiles of the sample of SE supernovae with signatures of a bipolar explosion used in this work, as well as their anticorrelation. Including other ingredients (clumpy structure, centrally concentrated density profile or non-axisymmetry) and radiative transfer effects may better capture the substructures of the profiles, but the bulk properties, that is, a single peak versus a double peak, should not be substantially affected.

Connection with GRBs

Although we excluded supernovae associated with a GRB from our analysis in the main text, the following events are closely examined in this section. It has been suggested that SN 1998bw, associated with GRB 980425, was viewed on-axis, whereas SN 2012ap, also associated with a GRB, was viewed off-axis[37,38,41,42]. Existing knowledge on the orientation of these two objects allowed us to employ them as test cases to evaluate the predictions made by the model developed in this work.

The [O I] and [Ca II] profiles of SN 1998bw and SN 2012ap are shown in Supplementary Fig. 5. The spectra were observed on 26 November 1998 (220 days after the explosion[49]) and 16 November 2012 (272 days after the explosion[41]), respectively. The [O I] profile of SN 1998bw appears to be single-peaked, whereas that of SN 2012ap has a trough at ~0 km s^{-1}, and is, therefore, classified as double-peaked. Although the [O I] profiles of both objects are aligned with the model predictions, their [Ca II] profiles exhibit peculiar characteristics. For SN 1998bw, [Ca II] appears to be flat-topped with a trough centred at −2,500 km s^{-1}. The overall shape resembles the [Ca II] profile of SN 2002ap, a prototype of a flat-topped profile, except for the large blueshift. If the trough is viewed as the centre of [Ca II], the explosion of SN 1998bw must be highly aspherical, which cannot be explained by the axisymmetric model in this work. In any case, the trough of the double-peaked [Ca II] was predicted to be at ~0 km s^{-1}. The lack of a [Ca II] flux at the redder wing suggests that the burning ash is either highly opaque, thus trapping the photons from the rear side, or is unipolar[4]. Additionally, the [Ca II] complex of SN 1998bw was also found to be blended by strong [Fe I] λ7155 at its blue wing, which is typically very weak in normal SE supernovae. These factors complicate the backward inference of the geometry of the explosion-made region from the [Ca II] profile. Regarding SN 2012ap, its [Ca II] is single-peaked but much broader than [O I]. A possible explanation for this broadening is contamination by the emissions from the iron-peak elements. However, the [Ca II] of this object is too broad for the de-blending procedure employed in this work.

To illustrate these points, the model profiles were compared with SN 1998bw and SN 2012ap. We fixed the viewing angle to $\theta = 0°$ (SN 1998bw) and $\theta = 75°$ (SN 2012ap) and then adjusted V_{max} until the widths of the observed and model [O I] matched. Although the [O I] profiles of both objects were well reproduced, the model [Ca II] failed to capture the main features of the observed [Ca II], as illustrated in Supplementary Fig. 5. For SN 2012ap, if we assumed that Fe and Ni have the same spatial distribution as the Ca and then adjusted the intensity ratios of the lines ($L_{7155}/L_{7291} \simeq 0.56$, $L_{7377}/L_{7291} \simeq 0.12$ and $L_{7412}/L_{7291} \simeq 0.31$), the observed [Ca II] complex can be reproduced to some extent. Note that the model profiles are blueshifted by 1,000 km s^{-1} to match the peak of the observed profile. However, introducing these emissions cannot explain the peculiar [Ca II] profile of SN 1998bw. In any case, the model profiles are too broad.

The failure in reproducing the [Ca II] profile of SN 1998bw suggests that the axisymmetric model may be overly simplified to explain the explosion geometry of GRB-associated supernovae. Further, the unusually abundance of iron-peak elements seen in both objects indicates that there were notable differences in explosive nucleosynthesis compared to normal SE supernovae. These observations, coupled with the absence of a GRB association for normal SE supernovae even when viewed on-axis, suggest that a bipolar explosion alone may not be sufficient to generate a GRB. More extreme conditions are probably required.

Peculiar object: SN 2015ah

SN 2015ah is classified as an OSCaD object, with the [Ca II] complex having a horn-like profile with a trough at ~4,000 km s^{-1}, like the central wavelength of [Ni II] λ7377 (~3,600 km s^{-1}). There is also a shallow trough at the central wavelength of [Fe II] λ7155 (~ −5,600 km s^{-1}). These features suggest that this complex is probably not dominated by [Ca II], unlike the rest of the sample. Instead, [Ni II] may be the main contributor. Both the [Fe I] and [Ni II] lines are emitted from the burning ash. Assuming that they share the same spatial distribution as the [Ca II]-emitting region, by adjusting the intensity ratios of the lines ($L_{7377}/L_{7291} \simeq 3.7$ and $L_{7155}/L_{7291} \simeq 1.1$), the model indeed reproduces the profile of the [Ca II] complex, as shown in Supplementary Fig. 6.

The strong [Ni II] ($L_{7377}/L_{7155} \simeq 3.4$) suggests that this object exhibits substantial overproduction of the Ni/Fe ratio[46,47]. To our knowledge, this is the third CC supernova that has been reported to have such a super-solar Ni/Fe ratio. The other two cases are SN 2012ec (ref. 47) and SN 2006aj (ref. 50). Although this sample is very small, it seems that an excess of the Ni/Fe ratio can occur for all types of CC supernova, irrespective of the presence or absence of the outer envelope. Further, two out of the three cases, SN 2006aj and SN 2015ah, are likely associated with non-spherical explosions, as an asymmetry in the explosion can effectively eject the deep-lying burning ash, leading to the change in the Ni/Fe ratio[3]. A systematic investigation of the relations between the Ni/Fe ratio and the properties of the explosion will be important to reveal the origin of the iron-peak elements and provide constraints on the explosion mechanism of CC supernovae.

Data availability

Most of the spectra are available from WiseRep (https://www.wiserep.org/) and Supernova Database of Berkeley (http://heracles.astro.berkeley.edu/sndb/). The data that support the plots within this paper and other findings of this study are available from the corresponding author upon reasonable request.

Code availability

Astropy, Matplotlib, Numpy and Scipy are available from the Python Package Index (PyPI) (https://pypi.org/). Upon request, the first author will provide the Python code used to generate the model line profiles.

References

1. Khokhlov, A. M. et al. Jet-induced explosions of core collapse supernovae. *Astrophys. J. Lett.* **524**, L107–L110 (1997).
2. Wang, L. et al. Bipolar supernova explosions. *Astrophys. J. Lett.* **550**, 1030–1035 (2001).
3. Maeda, K. & Nomoto, K. Bipolar supernova explosions: nucleosynthesis and implications for abundances in extremely metal-poor stars. *Astrophys. J.* **598**, 1163–1200 (2003).

4. Maeda, K., Nomoto, K., Mazzali, P. A. & Deng, J. Nebular spectra of SN 1998bw revisited: detailed study by one- and two-dimensional models. *Astrophys. J.* **640**, 854–877 (2006).
5. Woosley, S. E. & Bloom, J. S. The supernova gamma-ray burst connection. *Annu. Rev. Astron. Astrophys.* **44**, 507–556 (2006).
6. Nomoto, K. I., Iwamoto, K. & Suzuki, T. The evolution and explosion of massive binary stars and type Ib-Ic-IIb-IIL supernovae. *Phys. Rep.* **256**, 173–191 (1995).
7. Mazzali, P. A. et al. An asymmetric energetic type Ic supernova viewed off-axis, and a link to gamma ray bursts. *Sci.* **308**, 1284–1287 (2005).
8. Maeda, K. et al. Explosive nucleosynthesis in aspherical hypernova explosions and late-time spectra of SN 1998bw. *Astrophys. J.* **565**, 405–412 (2002).
9. Maeda, K. et al. Asphericity in supernova explosions from late-time spectroscopy. *Sci.* **319**, 1220- (2008).
10. Modjaz, M. et al. Double-peaked oxygen lines are not rare in nebular spectra of core-collapse supernovae. *Astrophys. J. Lett.* **687**, L9 (2008).
11. Taubenberger, S. et al. Nebular emission-line profiles of type Ib/c supernovae – probing the ejecta asphericity. *Mon. Not. R. Astron. Soc.* **397**, 677–694 (2009).
12. Milisavljevic, D. et al. Doublets and double peaks: late-time [O I] λλ6300,6364 line profiles of stripped-envelope, core-collapse supernovae. *Astrophys. J.* **709**, 1343–1355 (2010).
13. Fang, Q. et al. Statistical properties of the nebular spectra of 103 stripped-envelope core-collapse supernovae. *Astrophys. J.* **928**, 151 (2022).
14. Jerkstrand, A. in *The Handbook of Supernovae* (eds Alsabti, A. W. & Murdin, P.) 795–842 (Springer International Publishing, 2017).
15. Dessart, L. et al. Nebular phase properties of supernova Ibc from He-star explosions. *Astron. Astrophys.* **656**, A61 (2021).
16. Prentice, S. J. et al. Oxygen and calcium nebular emission line relationships in core-collapse supernovae and Ca-rich transients. *Mon. Not. R. Astron. Soc.* **514**, 5686–5705 (2022).
17. van Baal, B. F. A. et al. Modelling supernova nebular lines in 3D with EXTRASS. *Mon. Not. R. Astron. Soc.* **523**, 954 (2023).
18. Maurer, J. I. et al. Characteristic velocities of stripped-envelope core-collapse supernova cores. *Mon. Not. R. Astron. Soc.* **402**, 161–172 (2010).
19. Fransson, C. & Chevalier, R. A. Late emission from supernovae – a window on stellar nucleosynthesis. *Astrophys. J.* **343**, 323 (1989).
20. Jerkstrand, A. et al. Late-time spectral line formation in type IIb supernovae, with application to SN 1993J, SN 2008ax, and SN 2011dh. *Astron. Astrophys.* **573**, A12 (2015).
21. Kuncarayakti, H. et al. Nebular phase observations of the type-Ib supernova iPTF13bvn favour a binary progenitor. *Astron. Astrophys.* **579**, A95 (2015).
22. Fang, Q. et al. A hybrid envelope-stripping mechanism for massive stars from supernova nebular spectroscopy. *Nat. Astron.* **3**, 434–439 (2019).
23. Dessart, L. et al. Modeling of the nebular-phase spectral evolution of stripped-envelope supernovae. New grids from 100 to 450 days. *Astron. Astrophys.* **677**, A7 (2023).
24. Fang, Q. & Maeda, K. Inferring the progenitor mass–kinetic energy relation of stripped-envelope core-collapse supernovae from nebular spectroscopy. *Astrophys. J.* **949**, 93 (2023).
25. Nakamura, K. et al. Systematic features of axisymmetric neutrino-driven core-collapse supernova models in multiple progenitors. *Publ. Astron. Soc. Jpn* **67**, 107 (2015).
26. Woosley, S. E., Heger, A. & Weaver, T. A. The evolution and explosion of massive stars. *Rev. Mod. Phys.* **74**, 1015–1071 (2002).
27. Limongi, M. & Chieffi, A. Evolution, explosion, and nucleosynthesis of core-collapse supernovae. *Astrophys. J.* **592**, 404–433 (2003).
28. Benjamin, D. J. et al. Redefine statistical significance. *Nat. Hum. Behav.* **2**, 6–10 (2018).
29. Burrows, A. & Vartanyan, D. Core-collapse supernova explosion theory. *Nature* **589**, 29–39 (2021).
30. Blondin, J. M., Mezzacappa, A. & DeMarino, C. Stability of standing accretion shocks, with an eye toward core-collapse supernovae. *Astrophys. J.* **584**, 971 (2003).
31. Fernández, R. Three-dimensional simulations of SASI- and convection-dominated core-collapse supernovae. *Mon. Not. R. Astron. Soc.* **452**, 2071 (2015).
32. Matsumoto, J. et al. 2D numerical study for magnetic field dependence of neutrino-driven core-collapse supernova models. *Mon. Not. R. Astron. Soc.* **499**, 4174–4194 (2020).
33. Varma, V., Müller, B. & Schneider, F. R. N. 3D simulations of strongly magnetized non-rotating supernovae: explosion dynamics and remnant properties. *Mon. Not. R. Astron. Soc.* **518**, 3622–3636 (2023).
34. Reichert, M. et al. Magnetorotational supernovae: a nucleosynthetic analysis of sophisticated 3D models. *Mon. Not. R. Astron. Soc.* **518**, 1557–1583 (2023).
35. Shivvers, I. et al. The Berkeley sample of stripped-envelope supernovae. *Mon. Not. R. Astron. Soc.* **482**, 1545–1556 (2019).
36. Yaron, O. & Gal-Yam, A. WISeREP – an interactive supernova data repository. *Publ. Astron. Soc. Pac.* **124**, 668–681 (2012).
37. Galama, T. J. et al. An unusual supernova in the error box of the γ-ray burst of 25 April 1998. *Nature* **395**, 670–672 (1998).
38. Iwamoto, K. et al. A hypernova model for the supernova associated with the γ-ray burst of 25 April 1998. *Nature* **395**, 672–674 (1998).
39. Pian, E. et al. An optical supernova associated with the X-ray flash XRF 060218. *Nature* **442**, 1011–1013 (2006).
40. Mazzali, P. A. et al. A neutron-star-driven X-ray flash associated with supernova SN 2006aj. *Nature* **442**, 1018–1020 (2006).
41. Milisavljevic, D. et al. The broad-lined type Ic SN 2012ap and the nature of relativistic supernovae lacking a gamma-ray burst detection. *Astrophys. J.* **799**, 51 (2015).
42. Chakraborti, S. et al. A missing-link in the supernova-GRB connection: the case of SN 2012ap. *Astrophys. J.* **805**, 187 (2015).
43. Maeda, K. et al. The unique type Ib supernova 2005bf at nebular phases: a possible birth event of a strongly magnetized neutron star. *Astrophys. J.* **666**, 1069–1082 (2007).
44. Makarov, D. et al. HyperLEDA. III. The catalogue of extragalactic distances. *Astron. Astrophys.* **570**, A13 (2014).
45. Fang, Q. & Maeda, K. The origin of the Hα-like structure in nebular spectra of type IIb supernovae. *Astrophys. J.* **864**, 47 (2018).
46. Jerkstrand, A. et al. Constraints on explosive silicon burning in core-collapse supernovae from measured Ni/Fe ratios. *Astrophys. J.* **807**, 110 (2015).
47. Jerkstrand, A. et al. Supersolar Ni/Fe production in the type IIp SN 2012ec. *Mon. Not. R. Astron. Soc.* **448**, 2482–2494 (2015).
48. Dong, S. et al. Type Ia supernovae with bimodal explosions are common – possible smoking gun for direct collisions of white dwarfs. *Mon. Not. R. Astron. Soc.* **454**, L61 (2015).
49. Patat, F. et al. The metamorphosis of SN 1998bw. *Astrophys. J.* **555**, 900 (2001).
50. Maeda, K. et al. SN 2006aj associated with XRF 060218 at late phases: nucleosynthesis signature of a neutron star-driven explosion. *Astrophys. J. Lett.* **658**, L5–L8 (2007).

Acknowledgements

We thank J. Jiang, S. Mattila and A. Jerkstrand for reviewing the presubmission manuscript and providing a number of constructive suggestions. Q.F. acknowledges support from the Japan Society for the Promotion of Science (JSPS) through KAKENHI grant 20J23342. K.M. acknowledges support from JSPS KAKENHI grants JP18H05223, JP20H00174 and JP20H04737. H.K. and T.N. are funded by the Research Council of Finland through projects 324504, 328898 and 353019. This work is supported by the JSPS Open Partnership Bilateral Joint Research Projects between Japan and Finland (K.M. and H.K.; JPJSBP120229923).

Author contributions

Q.F., K.M. and T.N. initialized the project. Q.F. led the nebular spectroscopy analysis, model construction and the manuscript preparation. K.M. organized the efforts to interpret the results and assisted in manuscript preparation. H.K. and T.N. contributed to the spectroscopy analysis and interpretations. All authors contributed to the discussions and editing the manuscript.

Competing interests

The authors declare no competing interests.

Additional information

Supplementary information The online version contains supplementary material available at https://doi.org/10.1038/s41550-023-02120-8.

Correspondence and requests for materials should be addressed to Qiliang Fang or Keiichi Maeda.

Peer review information *Nature Astronomy* thanks Vishnu Varma and the other, anonymous, reviewer(s) for their contribution to the peer review of this work.

Reprints and permissions information is available at www.nature.com/reprints.

Publisher's note Springer Nature remains neutral with regard to jurisdictional claims in published maps and institutional affiliations.

Springer Nature or its licensor (e.g. a society or other partner) holds exclusive rights to this article under a publishing agreement with the author(s) or other rightsholder(s); author self-archiving of the accepted manuscript version of this article is solely governed by the terms of such publishing agreement and applicable law.

© The Author(s), under exclusive licence to Springer Nature Limited 2023